

Doping effects in amorphous oxides

Fuji FUNABIKI,^{*,†} Toshio KAMIYA^{**} and Hideo HOSONO^{*,**}

^{*}Frontier Research Center, Tokyo Institute of Technology, 4259 Nagatsuta-cho, Midori-ku, Yokohama 226-8503, Japan

^{**}Materials and Structures Laboratory, Tokyo Institute of Technology, 4259 Nagatsuta-cho, Midori-ku, Yokohama 226-8503, Japan

Impurity doping of crystalline Si is one of the most striking techniques in semiconductor technology. A rigid and perfect crystalline lattice is prerequisite for effective doping. However, it has been reported to date that introducing a small amount of impurities drastically improves also the properties of amorphous materials. This paper reviews three pronounced doping effects on optical and electrical properties of amorphous oxides; i.e., (i) F-doping of silica glass to improve the vacuum-ultraviolet optical transmission and radiation toughness, (ii) codoping effects on solubility enhancement of rare earth ions in silica glass melt, and (iii) electron-carrier generation in transparent amorphous oxide semiconductors. It is emphasized that effectiveness of electron doping is determined by the magnitude of electron affinity and stabilization energy of a dopant. Importance of the local structure formed around a dopant ion and the location of conduction band minimum measured from the vacuum level is addressed to understand the doping effects in amorphous oxides.

©2012 The Ceramic Society of Japan. All rights reserved.

Key-words : Doping, Silica, Defect, Codoping, Rare earth, Amorphous materials, Semiconductor, Oxide

[Received August 20, 2012; Accepted September 7, 2012]

1. Introduction

Doping is an important technique for developing functional materials. It imparts various functions to parent materials, or improves their properties. Material properties are drastically modified by addition of a small amount of dopants. Transparent oxide ceramics, which are intrinsically insulating and optically inactive, are changed into electronically and/or optically active materials by doping if it works. Doping effects are remarkable in crystalline materials such as Si and perovskite-type materials. Many review articles have been published for crystalline oxides which are the major constituents for ceramic materials.

In the past 3 decades, various novel methods such as chemical/physical vapor deposition¹⁾ and sol-gel²⁾ have been applied for synthesis of amorphous oxides including optical glass fibers for optical communication, glass photomasks of lithography for VLSI, and transparent amorphous oxide semiconductors (TAOSs) for thin film transistors (TFTs).³⁾ These fabrication methods make it possible to dope amorphous oxides with active components which were impossible to incorporate into amorphous matrices at an equilibrium state. Amorphous oxide has several advantages over polycrystalline oxide; i.e., it has high optical transmittance, excellent homogeneity, and good workability because of its continuous and isotropic structure. Thereby, amorphous oxide is formed into various shapes of solids such as tubes, prisms, spheres, films,⁴⁾ and fibers⁵⁾ with huge volume and smooth surface. However, many distinct properties of the crystalline material disappear or become vague in the amorphous state because of lack of long-range structural order.^{6),7)}

In this paper, we review the role of doping in amorphous oxide, introducing several successful examples. The most successful example of doping is carrier doping of crystalline Si. Only a ppm order of impurity effectively controls the Fermi level from the center of the bandgap to the edge, controlling polarity of carrier

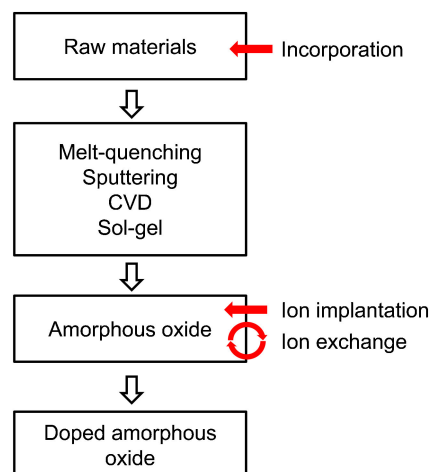


Fig. 1. (Color online) Three doping ways in amorphous oxides.

by a choice of impurity. This effectiveness is totally based on the presence of the crystalline lattice, and the incorporation of foreign atoms with a different number of valence electrons into the lattice site leads to the generation of free carriers. It is hard to expect such a dramatic effect from substitutional doping of amorphous oxides, but we consider some possibilities of effective doping of amorphous oxides based on their short-range structural order which is retained. We take three doping ways in amorphous oxides as summarized in Fig. 1; incorporation of a dopant as the raw material, introduction of doping elements into a bulk or surface region by ion implantation⁸⁾ and ion exchange.⁹⁾ The first one is a conventional route. The chemical compounds of transition metal,¹⁰⁾ rare earth (RE),¹¹⁾ and halogen¹²⁾ are incorporated into the starting raw materials. On the other hand, positively charged atoms are inserted by ion implantation under a non-equilibrium condition; i.e., they are embedded in interstitial positions of the target materials. Monovalent cations such as alkali ions are

[†] Corresponding author: F. Funabiki; E-mail: funabiki@lucid.msl.titech.ac.jp

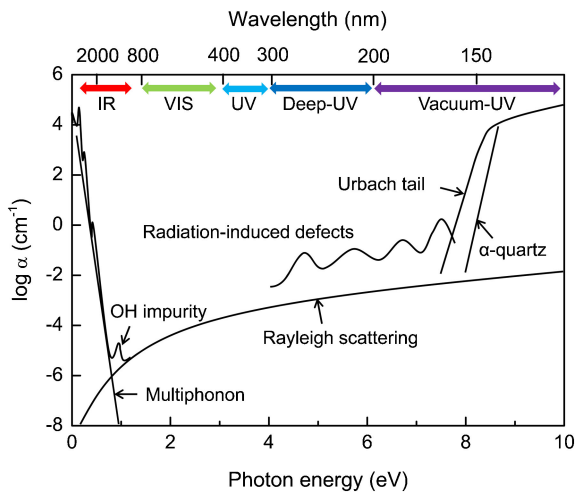


Fig. 2. (Color online) Origins of optical absorption in pure silica glass (schematic).

introduced into substitutional positions by the interdiffusion of ions (ion exchange). Strictly speaking, these dopings differ from the lattice doping defined in crystalline materials because, in the case of amorphous oxides, the local structure around a dopant relaxes largely upon doping. Because of this large relaxation, dopants do not remain at the original substitutional positions, and occupy off-center/interstitial positions. The introduction of dopants into interstitial positions is called chemical doping, and its most prominent example is electron doping of polyacetylene with iodine.¹³⁾

In general, the properties of amorphous materials are continuously changed with the chemical composition and are insensitive to the addition of a small amount of a certain component. This feature is advantageous to a fine tuning of the properties, but restricts the realization of outstanding properties or the nonlinear material design. Here we pick up three doping cases in amorphous oxides, i.e., F-doping of SiO₂ glass to improve the optical transparency in the vacuum-ultraviolet region, codoping of SiO₂ glass to enhance the solubility of optically active RE ion, and carrier doping of transparent amorphous oxide semiconductor to control the Fermi level. Each case is a successful example of doping.

2. Fluorine doping of silica glass

2.1 Discovery of fluorine doping

In 1970s, the study of silica glass fiber with a core-cladding structure has started for realizing ultra-low-loss optical fiber communication. Light signals propagate through the core part of fiber, reflecting at the core-clad boundary. To form a core-cladding structure, fluorine was added to a silica glass preform made by vapor-phase axial deposition¹⁴⁾ or a sol-gel method.¹⁵⁾ Fluorine has an effect to decrease the refractive index of silica glass in proportion to the concentration. Since silica glass shows low Rayleigh scattering and low-frequency multiphophonon absorption among oxide glasses, optical silica glass fiber enables an extremely long-distant information communication using $\sim 1.54\ \mu\text{m}$ light (see Fig. 2).^{16),17)} It was reported by several researches that the incorporation of several percent fluorine into silica glass decreases the viscosity of the glass melt by an order of magnitude,^{18),19)} and additionally, it shifts the optical transmittance edge of silica glass from $\sim 165\ \text{nm}$ to $<157\ \text{nm}$ in wavelength (Fig. 3),²⁰⁾⁻²²⁾ whereas changes in refractive index and

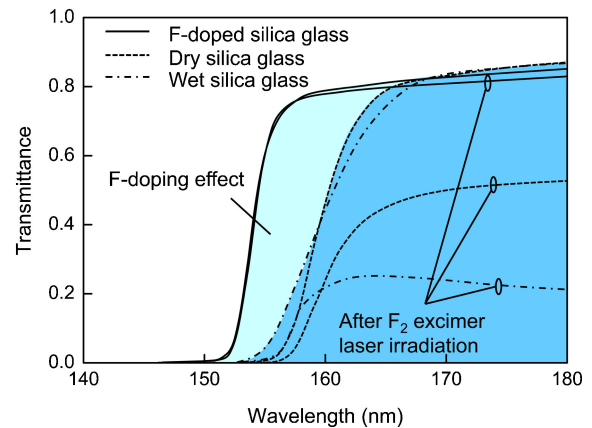


Fig. 3. (Color online) Optical transmittance spectra of wet, dry, and F-doped silica glasses before and after F₂ excimer laser irradiation at 157 nm (cited from ref. 21).

density remain within 1%. In 1980s, such F-doping effects had attracted much attention for fiber applications. Then, it was also found that F-doping improves the resistance to vacuum-ultraviolet (UV) light ($<200\ \text{nm}$)²¹⁾ and gamma-ray irradiation,²³⁾⁻²⁵⁾ and silica glass became available as optical materials for vacuum-UV applications, as shown in Fig. 3. At present, F-doped silica glasses are called “modified silica glass”, and used as photomask and lens materials. ‘Why is the optical property of silica glass much enhanced by the F-doping?’ To answer this question, the origins of vacuum-UV optical absorption in silica glass are explained in the next section.

2.2 Origins of optical absorption in silica glass

Silica glass was made from natural quartz and called fused quartz glass. Fused quartz glass contains many metal ion impurities such as Al, Ca, Na, Mg, and Fe, which degrade optical transparency. Then synthetic silica glass is prepared from high purity starting materials, which are obtained through a distillation process. Figure 2 shows an overview of the optical absorption of pure silica glass. There are three fundamental origins in the UV, visible, and infrared (IR) regions. The first origin is the interband transition between the valence band (mainly composed of oxygen 2p orbitals) and the conduction band (mainly Si 3s orbitals),²⁶⁾ the second one is the tail of Rayleigh scattering (optical loss) which comes from the density fluctuation in the bulk, and the last one is the multiphophonon excitation attributed to the vibrations (stretching and bending) of the Si–O–Si network.

In addition to these intrinsic origins, there are two additional origins resulting from the structural disorders of glass. One is the physical disorder, i.e., a wide variations in bond length and bond angle alters the electronic structure of silica, and gives rise to a large “Urbach tail” absorption below the bandgap.^{27),28)} The other is the chemical disorder which is defined as deviation from the short-range structure in crystalline SiO₂. That is, various types of point defects form localized states in the bandgap, and give Gaussian-like absorption bands below the Urbach tail. Figure 4 illustrates some examples of these absorption bands appearing in the UV region. The bandgap energy is $\sim 8.9\ \text{eV}$ for SiO₂ glass²⁹⁾ (determined by photoconductivity measurement), and is $\sim 9.2\ \text{eV}$ for α -quartz.³⁰⁾ The relation between the absorption coefficient (α) and the photon energy ($\hbar\omega$) is expressed by the following equation.

$$\alpha \propto (\hbar\omega - E_0)^2 / \hbar\omega \quad (1)$$

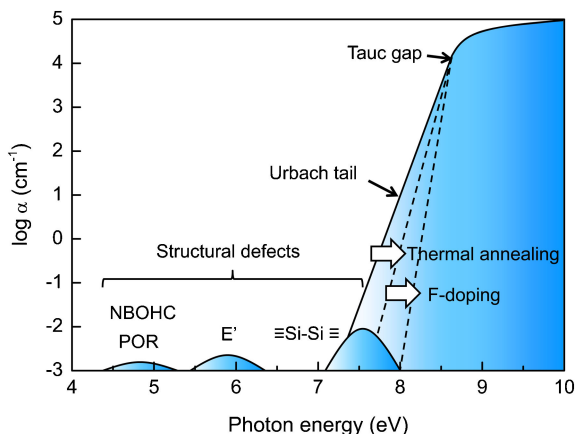


Fig. 4. (Color online) Optical absorption of silica glass due to the interband transition and point defects.

where Tauc gap^{28),31)} (optical bandgap, E_0) is obtained from the linear extrapolation of a measured $(\alpha\hbar\omega)^{1/2}-\hbar\omega$ plot. This gap is ~ 8.5 eV for SiO_2 glass, and is ~ 8.7 eV for α -quartz,²⁸⁾ where the α value exceeds 10^4 cm^{-1} regardless of the amorphous and crystalline states. On the other hand, the Urbach tail is expressed by the following equation.

$$\alpha \propto \exp(\hbar\omega/E_U) \quad (2)$$

Here, the minimum $\hbar\omega$ where Eq. (2) is valid is defined as the Urbach tail edge, and E_U is the Urbach energy. The Urbach tail is related directly to the degree of variations in bond length and bond angle; thus, the E_U of amorphous silica (~ 70 meV) is larger than that of quartz (~ 50 meV), and increases with temperature (~ 280 meV at 1900 K).²⁸⁾ Urbach tail edge is > 7.5 eV (< 165 nm) for SiO_2 glass,²⁸⁾ and is ~ 8.0 eV (~ 155 nm) for quartz³²⁾ at room temperature. This large difference between silica glass and quartz comes from physical disorder. On the other hand, point defects observed in silica glass are similar to interstitial-type and substitutional-type defects in quartz, which are a Si-Si bond ($\equiv\text{Si-Si}\equiv$), an E' center ($\equiv\text{Si}^*$), a non-bridging oxygen hole center ($\equiv\text{Si-O}^*$), a peroxy radical (O_2^- or $\equiv\text{Si-O-O}^*$), an interstitial O_2/O_3 , and so on.³³⁾ They give Gaussian-like bands below 7.6 eV. In most cases, their absorption coefficient is smaller than 10^{-1} cm^{-1} because of the low concentration ($< 10^{14}$ per cm^3), but is not negligible in long optical glass fibers. Moreover, the concentration is enhanced with the vacuum-UV light illumination.³⁴⁾⁻³⁶⁾ To understand the mechanism of the F-doping effects, these physical and chemical disorders in silica glass are explained in the next section.

2.3 Physical and chemical disorders in silica glass

The physical disorder is defined as the continuous variations in bond length and bond angle. In the case of SiO_2 glass, the physical disorder is correlated with the number of tetrahedral SiO_4 units in a silica ring. For example, since SiO_2 glass consists of three- to nine-membered rings,³⁷⁾ the Si-O-Si bond angle is distributed in the range from 120 to 180° (see Fig. 5), whereas the Si-O bond length and the O-Si-O bond angle are fixed in narrow variations even in the amorphous state due to their stiff potential.^{38),39)} The network of α -quartz is made only of six-membered rings (Si_6O_{18}), and the Si-O bond length, O-Si-O bond angle, and Si-O-Si bond angle take unique values of 1.61 Å, 109, and 144°, respectively, at room temperature. Therefore, the physical disorder is zero in α -quartz. The number of SiO_4 units in a silica ring depends on

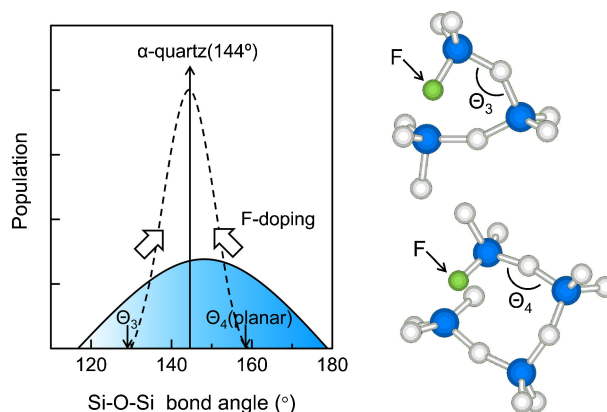
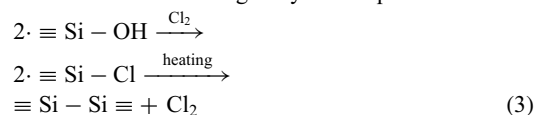


Fig. 5. (Color online) Distribution of Si-O-Si bond angle in silica glass and its narrowing by F-doping. The bond angles in the 3-/4-membered silica rings are denoted by Θ_3 and Θ_4 , respectively. These bond angles are rather deviated from the most stable angle ($\sim 144^\circ$).

fabrication condition, and is determined by the annealing temperature (in other words, fictive temperature, T_f). Low-temperature annealing has some effect to decrease the distribution, but a considerable distribution still remains because the relaxation rate quickly slows down as the temperature decreases.

On the other hand, the degree of the chemical disorder is proportional to the defect concentration. Most of the defects found in silica glass are oxygen-related ones; i.e., oxygen deficiency and oxygen interstitials. Representatives are the following four: a Si-Si bond,^{40),41)} an E' center,⁴²⁾ a non-bridging oxygen hole center (NBOHC),⁴³⁾ and a peroxy radical (O_2^- or $\equiv\text{Si-O-O}^*$).⁴⁴⁾ These defects are characterized by Gaussian-like optical absorptions around 7.6 eV, 5.8 eV, 4.8 eV, and 4.8 eV, respectively. They are mainly created during the sintering of a silica glass preform if they are not subjected to high energy radiation. Thus, the concentrations of these defects depend on the fabrication processes. “Water-free” silica glass has a large amount of the oxygen-deficient-type defects because of the following dehydration process.



2.4 Mechanism of F-doping effect

Several structural analyses have been carried out to reveal the mechanism of the F-doping effects. Youngman et al.^{45),46)} performed a nuclear magnetic resonance (NMR) study on ^{19}F and ^{29}Si in silica glass. They clarified that F ions substitute the oxygen ion sites to form tetrahedral SiO_3F units in silica glass. It was also clarified that a part of the SiO_3F units connects with a neighboring SiO_4 unit through the F ion and changes it into a SiO_4F unit with a five-fold coordinated Si. The percentage of the SiO_4F unit in the total fluorine concentration is, e.g., 15% at the 1.5 wt % F content. Shimodaira et al.^{47),48)} studied the Raman spectrum of F-doped silica glass, varying the F concentration and the fictive temperature (T_f). It was observed that the peak intensities of D_1 and D_2 originating from a four-membered ring (Si_4O_{12}) and a three-membered ring (Si_3O_9), respectively, were obviously reduced by decreasing T_f , where F-doping has an effect to decrease T_f because it reduces the viscosity of silica glass melt.^{18),19)} These results suggest that fluorine decreases the number of the 3-/4-membered rings in silica glass, changing the ring structures from closed to opened ones (Si_3FO_9 and $\text{Si}_4\text{FO}_{12}$) through the replacement of bridging Si-O-Si bond with non-bridging Si-F bond, as shown in

Fig. 5. Opening the 3-/4-membered rings composed of highly strained Si–O–Si bond and subsequent structural relaxation lead to reduction of physical disorder. As the result, the Urbach tail edge shifts from >7.5 to >7.9 eV, and Urbach energy is decreased from 104 to 58 meV by 570 wt. ppm F-doping.⁴⁹⁾

Hosono et al.²¹⁾ examined the radiation toughness of several silica glasses; F-doped silica glass, dry silica glass (the Si–OH content <1 ppm), and wet silica glass (the Si–OH content ~ 120 ppm). The concentration of the residual OH bond in the F-doped glass was close to that in the dry silica glass. In spite of the same level in the OH impurities, which absorb the UV light of 157 nm in wavelength, the F-doped silica glass exhibited an excellent resistance to an F₂ excimer laser (157 nm) as well as an ArF excimer laser (193 nm),¹⁴⁾ and even a better resistance to gamma ray.^{22)–24)} These results indicate that F-doping is effective to suppress the generation of point defects for irradiation of eximer lasers and high energy radiation. It should be noted that the Si–F bond (bond energy; 5.8 eV⁵⁰⁾) is much stronger than Si–O bond (4.7 eV⁵⁰⁾), i.e., F-doping relaxes the strained Si–O–Si bonds in the 3-/4-membered rings, and the energy levels of the resulting Si–F bonds are located below the Si–O bonds. Thus, holes generated by the band-to-band excitation are trapped neither at the Si–F bond nor on F. This is the reason why no defect associated with F is formed in the band gap of modified silica glass. Chlorine is effective to reduce the high temperature viscosity similar to fluorine, but enhances the radiation sensitivity. Since the Si–Cl bond (3.9 eV⁵⁰⁾) is weaker than the Si–O bond, their energy levels are located above the Si–O bonds. Thus, the holes generated by UV- or gamma-radiation are trapped at the Cl site, yielding Cl-associated color centers such as Cl₂[−].

3. Codoping of rare-earth-doped silica glass

3.1 Discovery of Nd–Al codoping

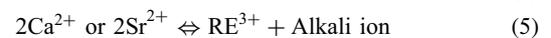
In 1970s, the study of optical glass fiber started to launch a telecommunication system. Among various fibers, a rare-earth (RE)-doped silica glass fiber with a core/cladding structure was reported for the first time by Stone and Burrus.⁵¹⁾ They added Nd₂O₃ and Al₂O₃ into the core part of fiber. Aluminum oxide was used to increase the refractive index of the silica glass core. They measured the photoluminescence spectrum of the Nd-activated glass fiber, and found that the luminescence spectrum shape was different between a Nd–Al-codoped fiber and a Nd-doped fiber, and moreover, the luminescence intensity of the Nd–Al-codoped fiber was stronger than that of the Nd-doped fiber. The reason had remained unclear for a decade. In 1980s, Arai et al.⁵²⁾ measured the density of Nd–Al-codoped silica glasses, and found that Nd–Al codoping brought about a negative volume change on mixing. This result indicated that in some manner, the Nd³⁺ ion and the Al³⁺ ion are correlated with each other in a silica network. They proposed a concept of “solvation shell” to explain this marked codoping effect. This finding attracted much attention because it revealed for the first time that codoping modifies the local environment around a RE ion in silica glass, and improves the luminescence properties drastically suppressing the concentration quenching. This discovery launched the study of codoping to improve the solubility of RE ion in silica glass. Various oxides of Al, P, B, Ge, and so on were examined as doping elements. It is indispensable to clarify the local structure around RE ions in oxide glass for understanding the microscopic mechanism.

3.2 Local structure around rare-earth ions

Rare-earth (RE) ions show sharp absorption and emission bands due to electric dipole f – f transitions. Although the f – f

transition is forbidden by the Laporte rule, it is allowed if the RE ion takes a non-centrosymmetric site. Various types of optical devices with 1.5 μ m light emission such as Er-doped fiber amplifiers,⁵³⁾ Er-doped waveguides,^{54),55)} and Er-doped microsphere lasers have been made by the incorporation of Er³⁺ ions into oxide glasses. Their optical performances strongly depend on the asymmetry of the crystal field around the Er³⁺. For example, the asymmetric crystal field enhances the spontaneous transition rate, and at the same time, decreases the luminescence lifetime. These two properties, which are inversely correlated, can be controlled by the energy transfer between two different RE ions such as Yb–Er, where Yb³⁺ has an intense and broad band at 800–1100 nm. This technique is also called codoping.

In the case of a crystalline oxide, RE-doping is generally performed by two types of atomic substitution accompanying a slight change of the short-range structure;



On the other hand, in an amorphous oxide, RE ions are introduced into the substitutional sites and/or interstitial sites of the host glass. However, large local structural relaxation occurs easily upon doping because of the presence of free volume. Thus, the local structure around RE ions is not so easy to predict from the short-range structure of the host glass. We need to consider the formation of a local structure in oxide glass melt. In the melt, RE ions are surrounded by more than six oxygen ions because of the large ionic radius.⁵⁶⁾ Because RE ions have high field strength⁵⁷⁾ and highly ionic bonding nature,⁵⁸⁾ similar to alkali ions and alkali-earth ions, they tend to be coordinated by non-bridging oxygen (NBO) ions, and the rest oxygen ions are bridging oxygen (BO) ions. By a disordered arrangement of BO and NBO with different negative valence charges, an asymmetric crystal field is formed around a RE ion. The degree of the asymmetry is estimated from the area intensity of the optical absorption bands of the RE ions by using a Judd-Ofelt analysis.^{59),60)} The local structure around a RE ion is considered to satisfy the charge neutrality requirement expressed by the following equation;

$$\sum_i n_i \frac{Z_i}{N_i} = 0 \quad (6)$$

where n_i is the number of chemical bond of the i -th ion forming the local structure, Z_i is the charge valence of the ion, and N_i is the coordination number of the ion. **Figure 6** shows an example of the local structure that satisfies the local charge neutrality requirement, but this structure, in which a RE ion is isolated in a silica network, is thermodynamically unstable as explained below.

In fiber optics, pure SiO₂ glass is preferable rather than a multi-component silicate glass because additive oxides increase both Rayleigh scattering and multi-phonon absorption. In addition, pure SiO₂ glass has advantages in mechanical strength, chemical durability, thermal stability, and so on. However, in the case of single component oxide glasses such as B₂O₃,^{61)–63)} SiO₂,^{64)–67)} and GeO₂,⁶³⁾ except P₂O₅ with NBOs, RE ions tend to form a RE-rich phase in the melts because there is no NBO, and as a consequent, the RE-containing glasses obtained are of phase-separated, that is, optically inhomogeneous and opaque. The solubility of rare-earth ion in silica glass is known to be <0.01 at. %.⁶⁷⁾ On the other hand, in multi-component glasses such as soda lime silicate glass, RE ions can be uniformly dissolved into the melts. That is, phase separation needs to be suppressed in silica glass melt to have a uniform RE-doped pure SiO₂ glass.

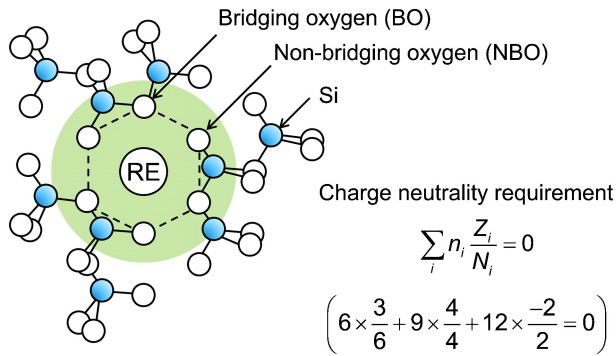


Fig. 6. (Color online) A hypothetical local structure model around rare-earth (RE) ion in silica glass.

3.3 Phase separation in RE₂O₃-SiO₂ glass melt

Rare-earth ions form a RE-rich phase in single component oxide glass melts because the ion having high field strength and a large coordination number needs to have many NBO ions to satisfy the local charge neutrality. This is a chemical explanation for the phase separation. On the other hand, thermodynamics provides us a physical explanation for the phase separation. Gibbs energy of mixing is expressed by the following equation

$$\Delta G_{\text{mix}} = \Delta H_{\text{mix}} - T \Delta S_{\text{mix}} \quad (7)$$

Because the RE-rich phases (REB₃O₆, RE₂Si₂O₇, RE₂Ge₂O₇, etc.) are very stable, enthalpy change of mixing (ΔH_{mix}) between the RE-rich phase and the pure oxide phase (B₂O₃, SiO₂, GeO₂, etc.) is very large while entropy change of mixing (ΔS_{mix}) remains small. Therefore, ΔG_{mix} is positive at a usual melting temperature (~1700 K). The positive ΔG_{mix} brings about the phase separation. The upper critical solution temperature (T_c) of RE₂O₃-B₂O₃ melts is above 2100 K,⁽⁶¹⁾⁻⁶³⁾ and that of the RE₂O₃-SiO₂ melts is above 2300 K.⁽⁶⁴⁾⁻⁶⁶⁾ Since the T_c is very high, homogeneous glass is not obtained unless a rapid quenching from the glass melt at $T > T_c$. Therefore, we need to reduce ΔH_{mix} or increase ΔS_{mix} for changing the sign of ΔG_{mix} (plus to minus) and inducing thermodynamical homogenization. In the next section, the role of codoping is discussed from these viewpoints.

3.4 Mechanism of codoping effect

Since Arai et al. reported in 1986, RE-doped silica glasses containing a small amount of Al₂O₃ have been studied by many authors. Morimo et al.⁽⁶⁸⁾ examined the local structure in Sm-Al-codoped SiO₂ glass using an extended X-ray absorption fine structure (EXAFS) spectroscopy. They found that while a peak due to a Sm-Sm pair correlation was observed for Sm-doped SiO₂ glass, only a Sm-Al correlation was observed instead of Sm-Sm for Sm-Al-codoped glass. This result confirmed that Al ion is correlated more preferably with Sm ion than Si ion. Since the elucidation of the oxygen coordination number of the incorporated Al ion is critical for considering the mechanism, several researchers have investigated the coordination number (i.e., 4 or 6). Fujiyama et al.⁽⁶⁹⁾ performed magic angle spinning (MAS)-NMR spectroscopy on Nd-Al-codoped SiO₂ glass prepared at 800°C using a sol-gel method, and reported that Al ion takes a distorted tetrahedral coordination, and Nd ion is stabilized by the distorted AlO₄ units. Sen⁽⁷⁰⁾ performed EXAFS spectroscopy on Nd-Al-codoped SiO₂ glass, and revealed that the oxygen coordination number of the Al was 4, and the Al-O distance was 1.76-1.77 Å. Monteil et al.⁽⁷¹⁾ performed molecu-

lar dynamics (MD) simulations of 18Er₂O₃·108Al₂O₃·1446SiO₂ glass with the assumption that the oxygen coordination number of Al was 4. The calculation showed that Er-Er clusters were still formed, and the number of the AlO₄ units surrounding an Er was 2. On the other hand, Wang et al.⁽⁷²⁾ proposed that the oxygen coordination number of Al should be 6 based on the coordination in alkali-free aluminosilicate crystals and glasses.^(73),74) Saitoh et al.⁽⁷⁵⁾ elucidated the local structure around an Er³⁺ ion using electron spin echo envelope modulation (ESEEM) spectroscopy. ESEEM spectroscopy is a powerful tool because it can determine the distance and coordination number of ligands in a medium-range structure because very fine interference signals, which are unresolved in conventional continuous wave (CW)-electron paramagnetic resonance (EPR) spectroscopy, are observable by time domain measurements; i.e., it provides information on the medium-range structure around a specific paramagnetic species and quantitative results are obtained by a simulation of the spectrum shape. Their results indicated that the oxygen coordination number of Al is primarily 6, and the number of AlO₆ unit surrounding an Er is 1. Lægsgaard⁽⁷⁶⁾ calculated the formation energy of α -quartz supercell composed of 24 TO₄ units (T=Al and Si) including M³⁺ ions (M=Er or Al) at the center of a six-membered ring. The formation energy of the supercell including an Er-Al complex (ErAl₃O₆) was larger than that including an Er-Er cluster (Er₂Si₂O₇) and an Al-Al cluster (Al₄O₆). This result suggests that the separation into the Er-Er cluster and the Al-Al cluster is more stable than the formation of the Er-Al complex. Therefore, he pointed out that the contribution of entropy is inevitable to explain the Er-Al codoping effect; i.e., the Al codoping increases ΔS_{mix} .⁽⁷⁶⁾ This idea is compatible with the fact that the incorporated Al³⁺ ion behaves as a network modifier; i.e., the coordination number is 6. It should be noted that the coordination number of Al in SiO₂ depends on its concentration; i.e., if the Al₂O₃ content is high, the 6-fold coordination is dominant, but the 4-fold coordination is found in the very low concentration (ppm level).⁽⁷⁷⁾

Phosphorus is also effective to enhance the dissolution of RE ions into silica glass melt. Canevali et al.⁽⁷⁸⁾ examined the local structures in B-, P-, B-P-, Ce-B-, Ce-P-, and Ce-B-P-codoped silica glasses using MAS-NMR and EPR spectroscopies. They found that P ion associated with Ce ion predominantly to form a Ce-P complex, and a triangular-pyramidal O=PO₃ unit was transformed into a tetrahedral PO₄ unit. On the other hand, the formation of Ce-B complex was not observed, and, instead, the segregation of CeO₂ was enhanced. Saitoh et al.⁽⁷⁵⁾ applied ESEEM spectroscopy and elucidated that a Ce ion was preferentially surrounded by four PO₄ units in the Ce-P-codoped silica glass while a Ce ion was surrounded by 0.8 BO₃ unit as speculated from the chemical composition of Ce-B-codoped silica glass.⁽⁷⁹⁾ They concluded that the coordination selectivity of the PO₄ unit to Ce is ~10 times larger than that of the SiO₄ unit, whereas the BO₃ unit has no selectivity (~1). **Figure 7** shows the photoluminescence spectra and the lifetime decay curves of Ce-P-codoped silica glass, Ce-doped calcium phosphate glass, and Ce-doped silica glass.⁽⁸⁰⁾ The photoluminescence peak energy and lifetime observed in Ce-P-codoped silica glass are quite different from those in Ce-doped silica glass, but are similar to those in Ce-doped phosphate glass because the local environment (crystal field) around Ce ions in silica glass is changed into that in phosphate glass by the solvation shell made of the PO₄ units.

Hereafter, we discuss the above codoping effects more comprehensively. **Figure 8** illustrates the change in enthalpy and entropy of an A-B system upon codoping with C. In the initial state, the

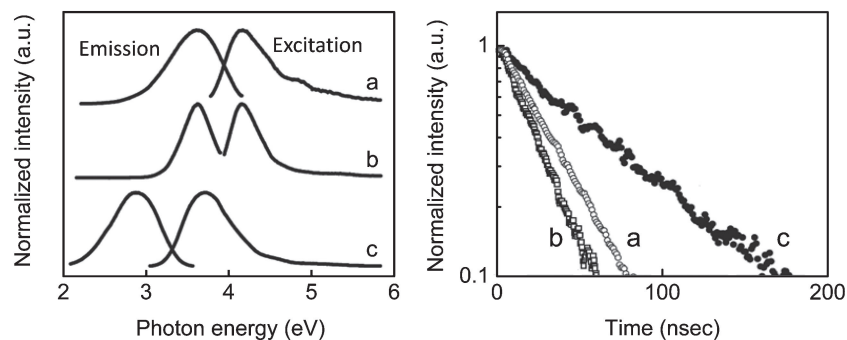


Fig. 7. Photoluminescence spectra and lifetime decay curves of Ce-P-codoped SiO_2 glass (a), Ce-doped $\text{CaO-P}_2\text{O}_5$ glass (b), and Ce-doped SiO_2 glass (c) (cited from ref. 80).

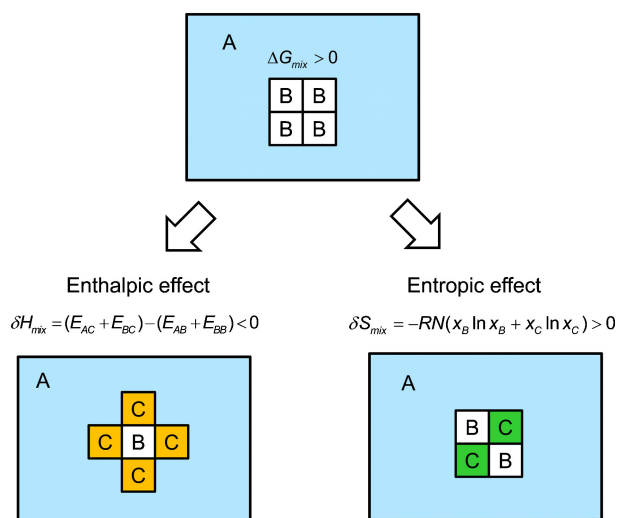


Fig. 8. (Color online) Change in enthalpy and entropy of A–B system upon codoping with C.

B cannot dissolve in the matrix A because of the large ΔG_{mix} . The formation of the solvation shell made of C on B decreases the enthalpy of the system, in which the large formation energy of A–B complexes (in other words, dissolution energy of B into A) is replaced by the small formation energy of A–C and B–C complexes, whereas entropy remains almost unchanged. This may be called enthalpic effect of codoping. On the other hand, entropy is increased by the addition of C having a similar local structure to B, whereas enthalpy is not changed because the dissolution energy is not different largely between B and C. This may be called entropic effect of codoping. Following this consideration, the roles of P- and Al-codopings are schematically shown in Fig. 9. Phosphorus ions form a solvation shell on a RE ion. The formation energy of RE–P and Si–P complexes appears to be smaller than those of RE–Si complexes because P ion has a NBO, and also has a tetrahedral coordination (TO_4) similar to Si ion. Therefore, RE–P codoping effectively reduces the immiscible temperature, and suppresses the phase separation. On the other hand, the formation energy of RE–Al and Si–Al complexes may be comparable with or larger than those of RE–Si complexes because a tetrahedral AlO_4 unit has no NBO. Instead, an octahedral AlO_6 unit has a similar local structure to RE (i.e., a large oxygen coordination number and the same charge state). The site sharing between Al and RE increases the entropy of glass melt, and as a result, phase separation is suppressed. Lastly, it is noted that B-codoping is less effective than Al- and P-

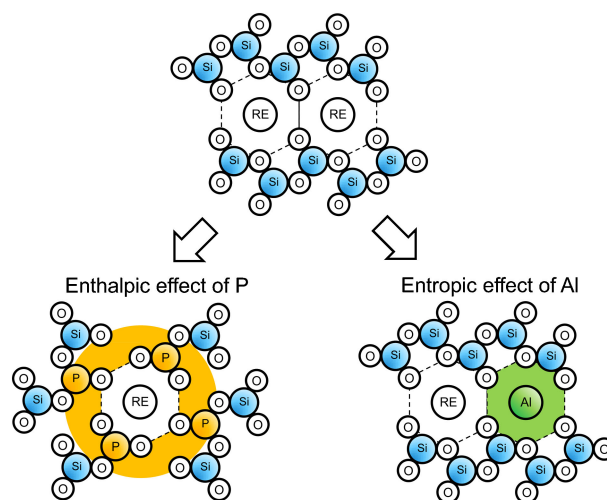


Fig. 9. (Color online) Change in enthalpy and entropy of rare-earth (RE)-containing silica glass upon codoping with P or Al.

codopings because B ion cannot share its own site with RE ion owing to the striking difference in the oxygen coordination number, and additionally, both BO_3 and BO_4 units have no NBO.

4. Electron doping of amorphous oxide

4.1 Transparent amorphous oxide semiconductor (TAOS)

As compared with covalent compounds such as Si (1.1 eV) and GaAs (1.4 eV), most non-transition metal oxides have wide bandgap energies over 3.0 eV because of the relatively high ionic nature in metal-oxygen bonds. In addition, it is difficult to form shallow donor levels in wide bandgap materials. As a result, many crystalline and the amorphous oxides of non-transition metals are transparent insulators. On the other hand, some of them such as In_2O_3 ⁸¹⁾ and ZnO ⁸²⁾ may be changed to transparent semiconductor or metallic conductor on the injection of mobile electrons. In 1996, Hosono et al.⁸³⁾ proposed that an electron-doped amorphous oxide composed of heavy metal cations with $(n-1)d^{10}\cdot ns^0$ electron configurations can be an excellent n-type semiconductor with a large electron mobility, $> 10 \text{ cm}^2\text{V}^{-1}\text{s}^{-1}$. In 2004, Nomura et al.³⁾ reported a high performance thin film transistors (TFTs) using a transparent amorphous oxide semiconductor (TAOS), which is called a-IGZO composed of In_2O_3 , Ga_2O_3 , and ZnO . The a-IGZO TFT fabricated at room temperature exhibited 10–20 times larger electron mobility than that ($0.5\text{--}1 \text{ cm}^2\text{V}^{-1}\text{s}^{-1}$) of a-Si:H TFTs. They reported that the electron concentration in

a-IGZO is well controllable in a wide range from $\ll 10^{15}$ to 10^{20} cm^{-3} , and the Fermi level exceeds the mobility edge when the carrier concentration exceeds $\sim 10^{18} \text{ cm}^{-3}$. This report attracted much attention from the flat panel display industry to develop next-generation displays such as transparent/flexible/jumbo/fast/organic light-emitting diode (OLED) displays that require high performance TFT to control the picture pixels and drive peripheral circuits. Since then, the number of the reports on TAOS TFTs^{84)–87)} has rapidly increased, and TAOS occupies one of the major materials comparable to a-Si:H and amorphous chalcogenides in international community of amorphous semiconductors.⁸⁸⁾

4.2 Electron conduction in TAOS

The effective mass of mobile electron depends largely on the size and the spatial directivity of relevant atomic orbitals and their connectivity (in other words, the variation of transfer integrals). If the conduction band is formed by largely spread ns orbitals ($n \geq 5$), the electron may have a small effective mass even in an amorphous state because the magnitude of the overlap between these neighboring s -orbitals is insensitive to the physical disorder (see Chapter 2.3). Oppositely, the electron mobility in silicon suffers from the disordered structure by a factor of a thousand because the magnitude of overlap between highly directional sp^3 – sp^3 bonding is largely affected from the variation in Si–Si–Si bond angle. A similar argument is valid for bronze oxides^{89)–91)} whose conduction band is composed of $4d$ or $5d$ orbitals in transition metals because the largely spread d orbital is similar to the largely spread s -orbitals in shape. **Figure 10** illustrates the difference in orbital overlap at the conduction band bottom between the crystalline states and the amorphous states of silicon and IGZO. In addition to the effective mass of the electrons, the dopant which supplies the carrier electrons is the important factor to control the electrical properties of a semiconductor. The concentration and the mobility of conductive electrons are related with their chemical potential, namely, Fermi energy (E_F), as expressed by the following equations using a nearly-free electron model.

$$n = 2 \left(\frac{2\pi m^* kT}{h^2} \right)^{3/2} \exp\left(-\frac{E_C - E_F}{kT}\right) \quad (8)$$

$$\mu = \frac{e\tau}{m^*} \quad (9)$$

where n is the mobile electron concentration, m^* is the effective mass, E_C is the conduction band mobility edge energy, μ is the

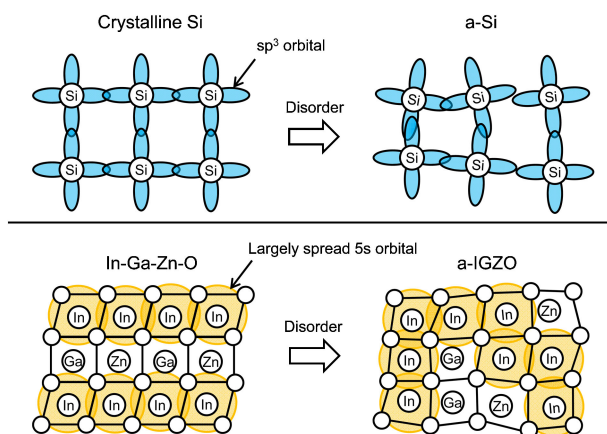


Fig. 10. (Color online) Difference in orbital overlap at conduction band bottom between crystalline and amorphous states of silicon and In-Ga-Zn-O.

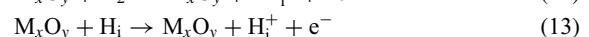
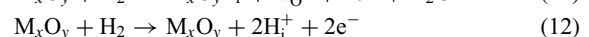
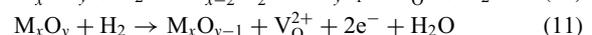
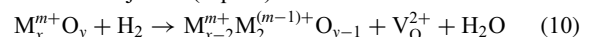
electron mobility, and τ is the momentum relaxation time. It indicates that it is important to raise E_F close to E_C to change a wide bandgap material from an insulator to a semiconductor, and ‘how to raise E_F ’ is the essential challenge.

4.3 Doping of TAOS

Substitutional doping, which is common in crystalline solids, is not effectively realized in an amorphous material because it has no well-defined atomic site (note a-Si⁹²⁾ is an exception). Thereby, carrier doping in an amorphous material should usually be regarded as off-stoichiometry of total ion charge⁹³⁾ and interstitial doping (chemical doping). The most successful example is iodine-doped polyacetylene.¹³⁾ The driving force is the net energy gain rising from charge transfer between related chemical species before and after doping. Neutral chemical species are introduced into or extracted from a target material, and it often induces charge transfer and creates donor/acceptor states. In the case of crystalline metal oxides, several interstitial defects (M_i , O_i) are created by the introduction of metal (M) and oxygen (O) atoms into the interstitial sites, and several atomic vacancies (V_M , V_O) are created by extracting the constituent atoms. For amorphous materials, ‘interstitial’ concept would be applied if such defects are introduced after the formation of the network structure e.g. by post-fabrication annealing and ion implantation. Considering their formation energies (net energy gain), the atomic radius of M_i should be small, and in addition, V_M is difficult to create compared with the other ones.^{94),95)} Therefore, favorable defects of TAOS are hydrogen (H_i)^{93),96)–98)} and oxygen deficiency (V_O).⁹⁹⁾ The both are donor-type defects. It is noted that in some cases, they act as sub-bandgap defects or electron traps, not as donors, as will be explained in the next section. Since hydrogen has a small atomic radius, it invades deeply using various chemical forms such as H^+ , H^0 , H^- , and H_2 . On the other hand, oxygen deficiency is easily created at a low oxygen partial pressure in the thin-film growth process or by reducing post-fabrication treatments, and it has three different charge states; V_O^X , V_O^+ , and V_O^{2+} . Electrical property of amorphous oxides is modified by these species.

4.4 Mechanism of electron doping

Because of the smallest atomic radius, hydrogen can invade a metal-oxygen structure through various routes. H_2 , a gas form of hydrogen, has an effect to reduce the valence of cations if valence changeable cations such as transition metal ions are included (Eq. 10). Moreover, when such a metal ion is not included, divalent oxygen vacancy (V_O^{2+}) with two free electrons may be formed (Eq. 11).¹⁰⁰⁾ When partial H_2 pressure is very high, and the environment temperature is also high, H_2 molecule invades oxides deeply, and may create isolated H_i atoms at interstitials (Eq. 12).¹⁰¹⁾ This situation is similar to the result of ion implantation,^{89),96)} in which positively charged ions such as H^+ , Li^+ , and Ag^+ are implanted into oxide substrates by a high accelerating voltage, and simultaneously, charge-compensating electrons are injected (Eq. 13).



Interstitial hydrogen atom (H_i) of the last two cases acts as donor. Its ionization supplies an electron. The formation energy of interstitial hydrogen with the charge q is estimated by the following relation;⁹⁴⁾

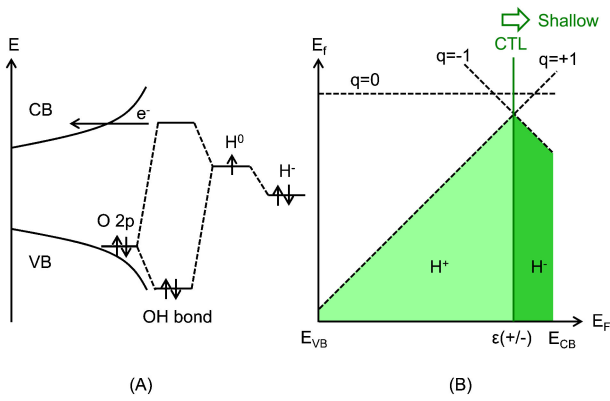


Fig. 11. (Color online) Schematics of energy levels (A) and charge diagram (B) of interstitial hydrogen introduced into metal oxide. CTL: charge transition level, CB: conduction band, VB: valence band, E_f : formation energy, E_f : Fermi energy.

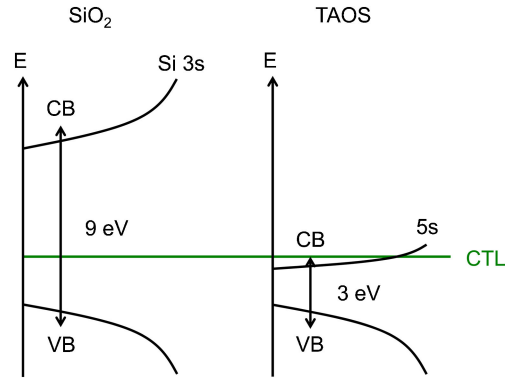


Fig. 13. (Color online) Difference in charge transition level (CTL) between SiO_2 and transparent amorphous oxide semiconductor (TAOS). CB: conduction band, VB: valence band.

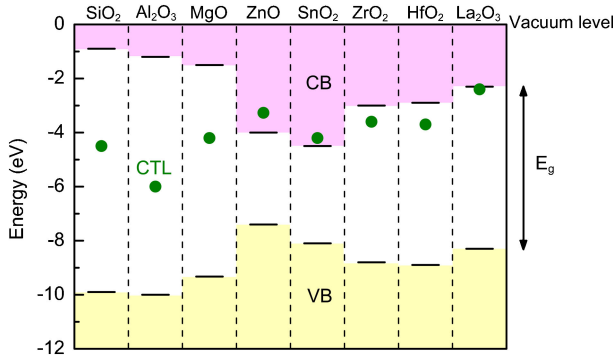


Fig. 12. (Color online) Charge transition level (CTL) of hydrogen in several relevant oxides (data are taken from Ref. 97). CB: conduction band, VB: valence band.

$$E_f(q) = E_{\text{MOH},q} - E_{\text{MO}} - \mu_{\text{H}} + qE_f \quad (14)$$

where q is the charge state of hydrogen, i.e., $q = +1, 0, -1$ for $\text{H}_i^+, \text{H}_i^0, \text{H}_i^-$, respectively. This formation energy is calculated from the total energies of hydrogenated and non-hydrogenated supercells (E_{MOH} and E_{MO}), chemical potential of hydrogen (μ_{H}), and the Fermi energy (E_f). **Figure 11** shows the schematics of energy levels and charge diagram of hydrogen, in which the intersection point of $E_f(+1)$ and $E_f(-1)$ represents the charge transition level (CTL), $\varepsilon(+/-)$, and the charge state of H_i is separated by the CTL, at which H_i is oxidized to H_i^+ or reduced to H_i^- . The neutral H_i^0 state is unfavorable because of the very high $E_f(0)$. This figure indicates that the incorporated hydrogen atom with a high CTL acts as a shallow donor when the energy level of H_i^+ is much lower than that of H_i^- . **Figure 12** shows the calculated CTL of hydrogen in several oxides reported in the literature.⁹⁷⁾ It is found that low conduction band (CB) minimum measured from the vacuum level (i.e., large electron affinity) is required to form shallow donor states because the $\varepsilon(+/-)$ level of hydrogen remains deep below the vacuum level. Because TAOS has a low CB minimum, it can change into semiconductor, which is totally different from SiO_2 (**Fig. 13**). For a-IGZO, Kamiya et al.¹⁰²⁾ have calculated the energy levels of hydrogen locating at various positions. In all models, the hydrogens form OH bonds and are ionized to H^+ , generating mobile electrons and raising E_f to above the CB minimum. In this, the model of hydrogen locating at near three-fold coordi-

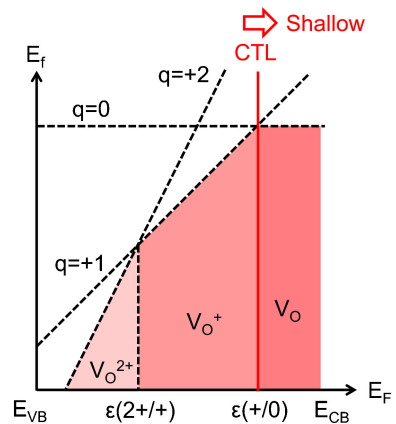
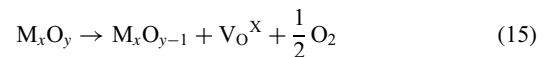


Fig. 14. (Color online) Schematics of charge diagram of oxygen vacancy in metal oxide. CTL: charge transition level, CB: conduction band, VB: valence band, E_f : formation energy, E_f : Fermi energy.

nated oxygen supplies an electron in higher energy level than that at near two-fold oxygen. Thus, a choice of material system is vital to the successful hydrogen doping.

In crystalline metal oxides, the constituent metal and oxygen atoms form metal-oxygen polyhedrons, and the oxygen connects the two or three metal atoms (M–O–M). Oxygen vacancy (M– V_O –M) is created at a low oxygen partial pressure during thermal annealing and thin-film growth. The amount of oxygen deficiency is equal to an off-stoichiometric chemical composition if the numbers of the metal cations are not changed;



Following the same manner to hydrogen, the formation energy of V_O with the charge q is evaluated by the following equation.

$$E_f(q) = E_{\text{MO}-1,q} - E_{\text{MO}} + \mu_\text{O} + qE_f \quad (16)$$

Figure 14 shows the schematics of charge diagram of oxygen vacancy, drawn by the lines of $E_f(+2)$, $E_f(+1)$, and $E_f(0)$. It is indicated that when the energy level of V_O^+ (an electron is trapped) or V_O^{2+} (void) is much lower than that of V_O^x (two electrons are trapped), the introduced oxygen vacancies may supply free electrons in high energy level to the CB. Oppositely, if the material contains void structures with a large free space like an oxygen vacancy, the free spaces form additional quantum-well-like electronic levels and trap the generated electrons, keeping the material insulating. For a long time, oxygen vacancy

is considered as the origin of electron carrier in ZnO_{1-x} , $\text{In}_2\text{O}_{3-x}$, and other crystalline oxide conductors. However, since 2000s, many authors^{103,104} have reported based on first-principles calculations that oxygen vacancy does not form a shallow donor state in the bulk of ZnO, in which CTL of V_{O} is below the middle of bandgap (bronze oxides^{105,106} with d -band conduction are excluded). Metal-related defects such as M_i and M_{O} (anti-site defect) can act as donors, but they are not favorable because of the high formation energy.¹⁰⁷ From these points, several authors suspected the possibility of hydrogen impurity at oxygen vacancies (i.e., H_{O}). In their calculations, substitutional hydrogen atom is a shallow donor. For a-IGZO, Kamiya et al.^{108,109} have calculated the energy levels of oxygen deficiency with various local structure models with the densities of 5.5–6.0 g/cm³ (c.f., 6.38 g/cm³ for c-IGZO). As the density increases, the void structure (free space) decreases, and E_{F} shifts from the deep level (0.4–1 eV above the valence band maximum) to the CB side and exceeds the CB minimum. In the case of the models with low densities, they contain a large portion of free space and form electron traps, indicating that the electron doping strongly depends on the fabrication condition.

5. Perspective

Successful examples of doping of amorphous oxides were described along with the respective mechanisms. Amorphous materials are commonly characterized by lack of long-range structural order, and there is a wide range of structural randomness strongly depending on material systems and fabrication conditions. Some types of amorphous materials have local structures similar to those in the corresponding crystalline phases. Substitutional doping would work to some extent for such a material system like amorphous silicon,⁹² but off-stoichiometry/interstitial doping is much more effective in general for carrier generation. In amorphous oxides, electron doping is possible like in the crystalline oxides when the stabilization energy of dopant is large, the CB minimum is located far from the vacuum level, and cation-anion stoichiometry is maintained. A cation which forms a stronger bond with constituent oxygen works as an effective dopant. Interstitial H ion is a typical example as demonstrated in TAOS thin films by ion implantation^{89,96,110} and hydrogen annealing.^{98,100} Here, we should consider what the essential bottleneck of the doping ability is. If it is determined by an average structure like chemical composition, a further improvement would be impossible. In silica glass, the minor strained Si–O bonds responsible for the tail state control the optical transmission in the vacuum-UV region. The concentration of such a strained bond is as low as ~1% estimated from the Raman spectral data.¹¹¹ This explains well why a small amount of fluorine improves the vacuum-UV transmittance. The same argument is valid for the codoping effects of P and Al to enhance the solubility of RE ion in silica glass melt.

Finally, we would like to mention about an example in which electron doping would alter the bulk structure of amorphous material. $12\text{CaO}\cdot 7\text{Al}_2\text{O}_3$ (C12A7) is a typical transparent insulator, but all the O^{2-} , which accommodate in the crystallographic cages as the counter anion to compensate the positive charge of the cage framework structure, may be exchanged by electrons through certain physical/chemical reduction treatments, and the resulting material C12A7:e^- exhibits metallic conduction (conductivity at RT is 1,500 Scm⁻¹).¹¹² When this C12A7:e^- is melted at 1800 K under a very low oxygen pressure and quenched, we may have C12A7:e^- glass in which almost the same concentration ($\sim 10^{21}$ cm⁻³) of electrons occupy the inter-

stitial positions.¹¹³ The C12A7:e^- glass melt shows metallic conduction, whereas C12A7:e^- glass is a semiconductor showing a variable range hopping. The Raman spectrum of C12A7:e^- glass is distinctly different in the location of a major band from that of stoichiometric C12A7:O^{2-} glass, strongly suggesting that the presence of interstitial electrons causes a drastic structural change to the bulk structure which can be easily observed by the conventional measurements. This distinct structural difference probed by Raman spectroscopy reflects on a striking difference in glass transition temperature (T_{g}); i.e., 700°C for the C12A7:e^- glass and 860°C for the C12A7:O^{2-} glass. Here, it should be noted that the change of T_{g} in the $x\text{CaO}\cdot(100-x)\text{Al}_2\text{O}_3$ glass system is $\sim 20^\circ\text{C}$ with a variation of the CaO content in the whole glass formation range ($55 < x < 65$).¹¹⁴ The large reduction of T_{g} by the exchange of O^{2-} with electrons confirms that the structure of C12A7 glass melt is dramatically altered by electron doping.

Validity of the conventional additive rule for physical properties of amorphous materials makes us possible to easily design an amorphous material. However, one cannot expect a dramatic change of the properties as long as following this rule. It is our belief that the most crucial is to find an appropriate amorphous material in which dopant works well for realizing innovative new amorphous materials.

Acknowledgements FF was supported by the MEXT Advanced Photon Science Alliance and HH acknowledges the support from the MEXT Elements Strategy Initiative to Form Core Research Center.

References

- 1) E. M. Dianov and V. M. Mashinsky, *J. Lightwave Technol.*, **23**, 3500–3508 (2005).
- 2) S. Shibata, M. Yamane, K. Kamada, K. Ohta, K. Sasaki and H. Masuhara, *J. Sol-Gel Sci. Technol.*, **8**, 959–964 (1997).
- 3) K. Nomura, H. Ohta, A. Takagi, T. Kamiya, M. Hirano and H. Hosono, *Nature*, **432**, 488–492 (2004).
- 4) H. Yabuta, M. Sano, K. Abe, T. Aiba, T. Den, H. Kumomi, K. Nomura, T. Kamiya and H. Hosono, *Appl. Phys. Lett.*, **89**, 112123 (2006).
- 5) S. Sakaguchi and S. Todoroki, *J. Non-Cryst. Solids*, **244**, 232–237 (1999).
- 6) A. Roder, W. Kob and K. Binder, *J. Chem. Phys.*, **114**, 7602–7614 (2001).
- 7) D. L. Griscom, *J. Non-Cryst. Solids*, **73**, 51–77 (1985).
- 8) K. Fukumi, A. Chayahara, K. Kadono, T. Sakaguchi, Y. Horino, M. Miya, K. Fujii, J. Hayakawa and M. Satou, *J. Appl. Phys.*, **75**, 3075–3080 (1994).
- 9) D. K. Hale, *Nature*, **217**, 1115–1118 (1968).
- 10) J. Qiu, K. Miyauchi, Y. Kawamoto, N. Kitamura, J. Qiu and K. Hirao, *Appl. Phys. Lett.*, **81**, 394–396 (2002).
- 11) M. Yamazaki, Y. Yamamoto, S. Nagahama, N. Sawanobori, M. Mizuguchi and H. Hosono, *J. Non-Cryst. Solids*, **241**, 71–73 (1998).
- 12) H. Kakiuchida, N. Shimodaira, E. H. Sekiya, K. Saito and A. J. Ikushima, *Appl. Phys. Lett.*, **86**, 161907 (2005).
- 13) C. K. Chiang, C. R. Fincher, Y. W. Park, A. J. Heeger, H. Shirakawa, E. J. Louis, S. C. Gau and A. G. MacDiarmid, *Phys. Rev. Lett.*, **39**, 1098–1101 (1977).
- 14) M. Kyoto, Y. Ohoga, S. Ishikawa and Y. Ishiguro, *J. Mater. Sci.*, **28**, 2738–2744 (1993).
- 15) S. Shibata, T. Kitagawa and M. Horiguchi, *J. Non-Cryst. Solids*, **100**, 269–273 (1988).
- 16) D. L. Griscom, *J. Ceram. Soc. Japan*, **99**, 899–916 (1991).
- 17) K. Saito, M. Yamaguchi, H. Kakiuchida, A. J. Ikushima, K. Ohsono and Y. Kurosawa, *Appl. Phys. Lett.*, **83**, 5175–5177 (2003).

- 18) M. Ohashi, M. Tateda, K. Tajima and K. Shiraki, *Electron. Lett.*, **28**, 1008–1010 (1992).
- 19) K. Saito and A. J. Ikushima, *J. Appl. Phys.*, **91**, 4886–4890 (2002).
- 20) K. Tsukuma, N. Yamada, S. Kondo, K. Honda and H. Segawa, *J. Non-Cryst. Solids*, **127**, 191–196 (1991).
- 21) H. Hosono, M. Mizuguchi, H. Kawazoe and T. Ogawa, *Appl. Phys. Lett.*, **74**, 2755–2757 (1999).
- 22) C. M. Smith and L. A. Moore, *J. Fluor. Chem.*, **122**, 81–86 (2003).
- 23) K. Awazu, H. Kawazoe and K. Muta, *J. Appl. Phys.*, **69**, 4183–4188 (1991).
- 24) K. Arai, H. Imai, J. Isoya, H. Hosono, Y. Abe and H. Imagawa, *Phys. Rev. B*, **45**, 10818–10821 (1992).
- 25) K. Kajihara, M. Hirano, L. Skuja and H. Hosono, *Phys. Rev. B*, **78**, 094201 (2008).
- 26) R. P. Gupta, *Phys. Rev. B*, **32**, 8278–8292 (1985).
- 27) F. Urbach, *Phys. Rev.*, **92**, 1324 (1953).
- 28) K. Saito and A. J. Ikushima, *Phys. Rev. B*, **62**, 8584–8587 (2000).
- 29) T. H. DiStefano and D. E. Eastman, *Solid State Commun.*, **9**, 2259–2261 (1971).
- 30) M. Schluter and J. R. Chelikowsky, *Solid State Commun.*, **21**, 381–384 (1977).
- 31) J. Tauc and A. Menth, *J. Non-Cryst. Solids*, **8-10**, 569–585 (1972).
- 32) A. Anedda, C. M. Carbonaro, R. Corpino and A. Serpim, *J. Non-Cryst. Solids*, **245**, 183–189 (1999).
- 33) L. Skuja, *J. Non-Cryst. Solids*, **239**, 16–48 (1998).
- 34) H. Hosono and R. A. Weeks, *J. Non-Cryst. Solids*, **116**, 289–292 (1990).
- 35) K. Kajihara, L. Skuja, M. Hirano and H. Hosono, *Appl. Phys. Lett.*, **79**, 1757–1759 (2001).
- 36) L. Skuja, K. Kajihara, M. Hirano and H. Hosono, *Phys. Rev. B*, **84**, 205206 (2011).
- 37) A. Pasquarello and R. Car, *Phys. Rev. Lett.*, **80**, 5145–5147 (1998).
- 38) E. Dupree and R. F. Pettifer, *Nature*, **308**, 523–525 (1984).
- 39) J. P. Rino, I. Ebbsjo, R. K. Kalia, A. Nakano and P. Vashishta, *Phys. Rev. B*, **47**, 3053–3062 (1993).
- 40) H. Hosono, Y. Abe, H. Imagawa, H. Imai and K. Arai, *Phys. Rev. B*, **44**, 12043–12045 (1991).
- 41) M. Cannas, F. M. Gelardi, F. Pullara, M. Barbera, A. Collura and S. Varisco, *J. Non-Cryst. Solids*, **280**, 188–192 (2001).
- 42) H. Hosono, Y. Ikuta, T. Kinoshita, K. Kajihara and M. Hirano, *Phys. Rev. Lett.*, **87**, 175501 (2001).
- 43) K. Kajihara, L. Skuja, M. Hirano and H. Hosono, *J. Non-Cryst. Solids*, **345-346**, 219–223 (2004).
- 44) E. J. Friebele, D. L. Griscom and M. Stapelbroek, *Phys. Rev. Lett.*, **42**, 1346–1349 (1979).
- 45) R. E. Youngman and S. Sen, *J. Non-Cryst. Solids*, **337**, 182–186 (2004).
- 46) R. E. Youngman and S. Sen, *J. Non-Cryst. Solids*, **349**, 10–15 (2004).
- 47) N. Shimodaira, K. Saito and A. J. Ikushima, *J. Appl. Phys.*, **91**, 3522–3525 (2002).
- 48) N. Shimodaira, K. Saito, N. Hiramitsu, S. Matsushita and A. J. Ikushima, *Phys. Rev. B*, **71**, 024209 (2005).
- 49) L. Skuja, K. Kajihara, Y. Ikuta, M. Hirano and H. Hosono, *J. Non-Cryst. Solids*, **345-346**, 328–331 (2004).
- 50) J. E. Huheey, “Inorganic Chemistry”, 3rd Ed. by Harper and Row, New York (1983).
- 51) J. Stone and C. A. Burrus, *Appl. Phys. Lett.*, **23**, 388–389 (1973).
- 52) K. Arai, H. Namikawa, K. Kumata, T. Honda and Y. Ishii, *J. Appl. Phys.*, **59**, 3430–3436 (1986).
- 53) W. J. Miniscalco, *J. Lightwave Technol.*, **9**, 234–250 (1991).
- 54) D. L. Veasey, D. S. Funk, P. M. Peters, N. A. Sanford, G. E. Obarski, N. Fontaine, M. Young, A. P. Peskin, W. C. Liu, S. N. Houde-Walter and J. S. Hayden, *J. Non-Cryst. Solids*, **263-264**, 369–381 (2000).
- 55) S. F. Wong and E. Y. B. Pun, *IEEE Photon. Technol. Lett.*, **14**, 80–82 (2002).
- 56) M. A. Marcus and A. Polman, *J. Non-Cryst. Solids*, **136**, 260–265 (1991).
- 57) M. Poulain, *Nature*, **293**, 279–280 (1981).
- 58) G. de Leede and H. de Waal, *J. Non-Cryst. Solids*, **104**, 45–51 (1988).
- 59) B. R. Judd, *Phys. Rev.*, **127**, 750–761 (1962).
- 60) G. S. Ofelt, *J. Chem. Phys.*, **37**, 511–520 (1962).
- 61) E. M. Levin, *Phys. Chem. Glasses*, **7**, 90–93 (1966).
- 62) I. N. Chakraborty, D. E. Day, J. C. Lapp and J. E. Shelby, *J. Am. Ceram. Soc.*, **68**, 368–371 (1985).
- 63) P. Hudon and D. R. Baker, *J. Non-Cryst. Solids*, **303**, 354–371 (2002).
- 64) F. P. Glasser, I. Warshaw and R. Roy, *Phys. Chem. Glasses*, **1**, 39–45 (1960).
- 65) V. B. M. Hageman and H. A. J. Oonk, *Phys. Chem. Glasses*, **27**, 194–198 (1986).
- 66) V. McGahay and M. Tomozawa, *J. Non-Cryst. Solids*, **159**, 246–252 (1993).
- 67) M. W. Sckerl, S. Guldborg-Kjaer, M. R. Poulsen and P. Shi, *Phys. Rev. B*, **59**, 13494–13497 (1999).
- 68) R. Miromo, T. Mizushima, Y. Udagawa, N. Kakuta, A. Ueno and H. Okumura, *J. Electrochem. Soc.*, **137**, 2340–2343 (1990).
- 69) T. Fujiyama, T. Yokoyama, M. Hori and M. Sasaki, *J. Non-Cryst. Solids*, **135**, 198–203 (1991).
- 70) S. Sen, *J. Non-Cryst. Solids*, **261**, 226–236 (2000).
- 71) A. Monteil, S. Chaussedent, G. Alombert-Goget, N. Gaumer, J. Obriot, S. J. L. Ribeiro, Y. Messaddeq, A. Chiasera and M. Ferrari, *J. Non-Cryst. Solids*, **348**, 44–50 (2004).
- 72) J. Wang, W. S. Brocklesby, J. R. Lincoln, J. E. Townsend and D. N. Payne, *J. Non-Cryst. Solids*, **163**, 261–267 (1993).
- 73) M. Yamane and M. Okuyama, *J. Non-Cryst. Solids*, **52**, 217–226 (1982).
- 74) S. L. Lin and C. S. Hwang, *J. Non-Cryst. Solids*, **202**, 61–67 (1996).
- 75) A. Saitoh, S. Matsuishi, C. Se-Weon, J. Nishii, M. Oto, M. Hirano and H. Hosono, *J. Phys. Chem. B*, **110**, 7617–7620 (2006).
- 76) J. Lægsgaard, *Phys. Rev. B*, **65**, 174114 (2002).
- 77) K. L. Brower, *Phys. Rev. B*, **20**, 1799–1811 (1979).
- 78) C. Canevali, M. Mattoni, F. Morazzoni, R. Scotti, M. Casu, A. Musinu, R. Krsmanovic, S. Polizzi, A. Speghini and M. Bettinelli, *J. Am. Chem. Soc.*, **127**, 14681–14691 (2005).
- 79) A. Saitoh, S. Matsuishi, M. Oto, T. Miura, M. Hirano and H. Hosono, *Phys. Rev. B*, **72**, 212101 (2005).
- 80) A. Saitoh, S. Murata, S. Matsuishi, M. Oto, T. Miura, M. Hirano and H. Hosono, *Chem. Lett.*, **34**, 1116–1117 (2005).
- 81) J. Rosen and O. Warschkow, *Phys. Rev. B*, **80**, 115215 (2009).
- 82) E. V. Monakhov, J. S. Christensen, K. Maknys, B. G. Svensson and A. Yu. Kuznetsov, *Appl. Phys. Lett.*, **87**, 191910 (2005).
- 83) H. Hosono, M. Yasukawa and H. Kawazoe, *J. Non-Cryst. Solids*, **203**, 334–344 (1996).
- 84) J. K. Jeong, H. J. Chung, Y. G. Mo and H. D. Kim, *J. Electrochem. Soc.*, **155**, H873–H877 (2008).
- 85) S. Lee, S. Park, S. Kim, Y. Jeon, K. Jeon, J. H. Park, J. Park, I. Song, C. J. Kim, Y. Park, D. M. Kim and D. H. Kim, *IEEE Electron Device Lett.*, **31**, 231–233 (2010).
- 86) B. Kim, E. Chong, D. H. Kim, Y. W. Jeon, D. H. Kim and S. Y. Lee, *Appl. Phys. Lett.*, **99**, 062108 (2011).
- 87) T. T. Trinh, V. D. Nguyen, K. Ryu, K. Jang, W. Lee, S. Baek, J. Raja and J. Yi, *Semicond. Sci. Technol.*, **26**, 085012 (2011).
- 88) H. Hosono, *J. Non-Cryst. Solids*, **352**, 851–858 (2006).
- 89) H. Hosono, M. Miyakawa, H. Kawazoe and K. Shimizu, *J. Non-Cryst. Solids*, **241**, 190–194 (1998).

- 90) L. Chen, S. Shet, H. Tang, K. S. Ahn, H. Wang, Y. Yan, J. Turner and M. Al-Jassim, *J. Appl. Phys.*, **108**, 043502 (2010).
- 91) N. J. Podraza, B. D. Gauntt, M. A. Motyka, E. C. Dickey and M. W. Horn, *J. Appl. Phys.*, **111**, 073522 (2012).
- 92) W. E. Spear and P. G. Le Comber, *Solid State Commun.*, **88**, 1015–1018 (1993).
- 93) T. Kamiya, K. Nomura and H. Hosono, *J. Display Technol.*, **5**, 273–288 (2009).
- 94) F. Oba, A. Togo, I. Tanaka, J. Paier and G. Kresse, *Phys. Rev. B*, **77**, 245202 (2008).
- 95) T. Kamiya, K. Nomura and H. Hosono, *Sci. Technol. Adv. Mater.*, **11**, 044305 (2010).
- 96) H. Hosono, N. Kikuchi, N. Ueda, H. Kawazoe and K. Shimidzu, *Appl. Phys. Lett.*, **67**, 2663–2665 (1995).
- 97) K. Xiong, J. Robertson and S. J. Clark, *J. Appl. Phys.*, **102**, 083710 (2007).
- 98) L. Shao, K. Nomura, T. Kamiya and H. Hosono, *Electrochem. Solid-State Lett.*, **14**, H197–H200 (2011).
- 99) S. Lany and A. Zunger, *Phys. Rev. B*, **72**, 035215 (2005).
- 100) N. Ito, Y. Sato, P. K. Song, A. Kajjio, K. Inoue and Y. Shigesato, *Thin Solid Films*, **496**, 99–103 (2006).
- 101) S. W. Tsao, T. C. Chang, S. Y. Huang, M. C. Chen, S. C. Chen, C. T. Tsai, Y. J. Kuo, Y. C. Chen and W. C. Wu, *Solid-State Electron.*, **54**, 1497–1499 (2010).
- 102) T. Kamiya, K. Nomura and H. Hosono, *Phys. Status Solidi., A Appl. Mater. Sci.*, **207**, 1698–1703 (2010).
- 103) I. Tanaka, F. Oba, K. Tatsumi, M. Kunisu, M. Nakano and H. Adachi, *Mater. Trans.*, **43**, 1426–1429 (2002).
- 104) A. Janotti and C. G. Van de Walle, *Appl. Phys. Lett.*, **87**, 122102 (2005).
- 105) W. J. Yin, S. H. Wei, M. M. Al-Jassim and Y. Yan, *Appl. Phys. Lett.*, **99**, 142109 (2011).
- 106) D. B. Migas, V. L. Shaposhnikov, V. N. Rodin and V. E. Borisenko, *J. Appl. Phys.*, **108**, 093713 (2010).
- 107) A. Janotti and C. G. Van de Walle, *Phys. Rev. B*, **76**, 165202 (2007).
- 108) T. Kamiya, K. Nomura, M. Hirano and H. Hosono, *Phys. Status Solidi., C Curr. Top. Solid State Phys.*, **5**, 3098–3100 (2008).
- 109) T. Kamiya, K. Nomura and H. Hosono, *Phys. Status Solidi., A Appl. Mater. Sci.*, **206**, 860–867 (2009).
- 110) S. Narushima, H. Hosono, J. Jisun, T. Yoko and K. Shimakawa, *J. Non-Cryst. Solids*, **274**, 313–318 (2000).
- 111) A. E. Geissberger and F. L. Galeener, *Phys. Rev. B*, **28**, 3266–3271 (1983).
- 112) S. Matsuishi, Y. Toda, M. Miyakawa, K. Hayashi, T. Kamiya, M. Hirano, I. Tanaka and H. Hosono, *Science*, **301**, 626–629 (2003).
- 113) S. W. Kim, T. Shimoyama and H. Hosono, *Science*, **333**, 71–74 (2011).
- 114) P. L. Higby, R. J. Ginther, I. D. Aggarwal and E. J. Friebele, *J. Non-Cryst. Solids*, **126**, 209–215 (1990).